Strongly correlated excitonic insulator in atomic double layers

Liguo Ma[1], Phuong X. Nguyen[1], Zefang Wang[1], Yongxin Zeng[2], Kenji Watanabe[3], Takashi Taniguchi[3], Allan H. MacDonald[2], Kin Fai Mak[1,4,5]*, Jie Shan[1,4,5]*

[1]School of Applied and Engineering Physics, Cornell University, Ithaca, NY, USA
[2]Department of Physics, University of Texas at Austin, Austin, TX, USA
[3]National Institute for Materials Science, Tsukuba, Japan
[4]Laboratory of Atomic and Solid State Physics, Cornell University, Ithaca, NY, USA
[5]Kavli Institute at Cornell for Nanoscale Science, Ithaca, NY, USA

*Email: jie.shan@cornell.edu; kinfai.mak@cornell.edu
These authors contributed equally: Liguo Ma and Phuong X. Nguyen.

Excitonic insulators (EIs) arise from the formation of bound electron-hole pairs (excitons) [1, 2] in semiconductors and provide a solid-state platform for quantum many-boson physics [3-8]. Strong exciton-exciton repulsion is expected to stabilize condensed superfluid and crystalline phases by suppressing both density and phase fluctuations [8-11]. Although spectroscopic signatures of EIs have been reported [6, 12-14], conclusive evidence for strongly correlated EI states has remained elusive. Here, we demonstrate a strongly correlated two-dimensional (2D) EI ground state formed in transition metal dichalcogenide (TMD) semiconductor double layers. A quasi-equilibrium spatially indirect exciton fluid is created when the bias voltage applied between the two electrically isolated TMD layers is tuned to a range that populates bound electron-hole pairs, but not free electrons or holes [15-17]. Capacitance measurements show that the fluid is exciton-compressible but charge-incompressible – direct thermodynamic evidence of the EI. The fluid is also strongly correlated with a dimensionless exciton coupling constant exceeding 10. We construct an exciton phase diagram that reveals both the Mott transition and interaction-stabilized quasi-condensation. Our experiment paves the path for realizing exotic quantum phases of excitons [8], as well as multi-terminal exciton circuitry for applications [18-20].

In bulk materials EIs can occur in small band gap semiconductors and small band overlap semimetals [21]. In the semiconductor limit, EIs occur when the electron-hole binding energy exceeds the charge band gap. The ground state exciton population is then determined by balancing the negative exciton formation energy against the mean exciton-exciton repulsion energy. Although the concept has been understood for sixty years, it has been challenging to establish distinct experimental signatures of its realization. One problem is that exciton coherence in condensed phases inevitably couples to the crystal Hamiltonian, disordered or not, so that condensation does not imply superfluidity [22]. A second problem is that the exciton population of a particular material depends very sensitively on band structure details and cannot be controlled. Here we solve both problems by establishing electrical control of the chemical potentials of excitons that are spatially indirect; the electron and hole wavefunctions do not interfere so that macroscopic phase coherence is spontaneous, allowing exciton superfluidity [15, 16, 23, 24].

We achieve these properties in TMD double layers, whose emergence has opened new paths to realize and control the many-exciton states [15-17, 23-32]. Both the formation of dipolar excitons (i.e. excitons with a permanent dipole) and the reduced dielectric screening of the electrostatic interactions favor strong exciton-exciton repulsion. Separate electrical contacts to isolated electron and hole layers provide a reservoir for interlayer excitons with a conveniently tunable chemical potential for thermodynamic measurements [15, 16, 24].

Exciton-contact devices

Consider TMD double layers with a type II band alignment and a spatially indirect band gap E_G (Fig. 1a). The conduction and valence band edges are located in two separate layers. The application of an interlayer bias voltage, V_b, splits the electron and hole electrochemical potentials and reduces the charge gap by eV_b (here e denotes the elementary charge). When the charge gap, $E_G - eV_b$, is below the exciton binding energy, E_B, formation of an interlayer exciton fluid is expected [15, 16, 24]. The exciton chemical potential is defined by $\mu_X = eV_b$ in thermal equilibrium, which is the sum of the electron and hole electrochemical potentials [15, 16, 24]. Because of the large exciton binding energies in atomically thin TMD semiconductors (10's – 100's meV) [23, 24, 32], exciton fluids with a widely tunable chemical potential are achievable.

TMD double layer devices with separate electrical contacts have been demonstrated recently [27, 28]. However, equilibrium interlayer exciton fluids whose thermodynamic properties could be studied have not been achieved previously. The earlier devices allowed substantial tunneling between the two layers and therefore operated only in the small tunnel junction resistance regime (that is, electrical contact resistances exceeded the tunnel junction resistance); the electron/hole layers could not be maintained at the same electrochemical potential as the contacts [16]. The new results employ a device design that allows us to reach the large tunnel junction resistance regime and demonstrate direct thermodynamic evidence of an EI ground state.

Figure 1b is a schematic device cross-section (see Methods for details on device fabrication). We choose monolayer $MoSe_2$ (Mo) as the electron layer and monolayer WSe_2 (W) as the hole layer. A hexagonal boron nitride (hBN) tunnel barrier separates the two TMDs, which are angle-misaligned. The structure is completed with symmetric top and bottom gates that consist of hBN gate dielectrics (~ 10 nm) and graphite gate electrodes. To achieve small contact resistances, we separate the device into a contact region and a region of interest. We heavily dope the contact region while keeping the region of interest charge neutral by employing different barrier thicknesses: 1-2 nm in the region of interest and ~ 10 nm in the contact region. When the device is subjected to anti-symmetric gating, $\Delta \equiv (V_{bg} - V_{tg})/2$, where V_{bg} and V_{tg} are the bottom and top gate voltages, respectively, a vertical electric field is generated. The field induces a large potential drop on the double layers in the contact region, which closes the band gap and introduces free carriers; the field reduces the band gap (but does not close it) in the region of interest. We achieve good electrical contacts down to 10-15 K. Unless otherwise specified, all results presented below are obtained at 15 K with $\Delta = 4.6$ V.

Compressibility measurements

We characterize the thermodynamic properties of the double layer, including both the exciton and charge compressibility, using the capacitance technique (Methods). The penetration capacitance per unit area, $C_P = e\frac{dn_{bg}}{dV_{tg}}$, measures the differential charge density on the bottom gate, dn_{bg}, induced by a small AC voltage, dV_{tg}, on the top gate (Fig. 1c). It characterizes how well the entire double layer screens an AC electric field and is approximately given by the charge compressibility (Methods).

Figure 1d shows C_P as a function of (symmetric) gating, $V_g \equiv (V_{tg} + V_{bg})/2$. It shifts the electron and hole chemical potentials together and controls the electron-hole density imbalance. Under zero bias the electrons and holes have the same chemical potential. When the chemical potential is inside the band gap of the double layer, the double layer is charge incompressible; C_P is given by the gate-to-gate geometrical capacitance, C_{gg}. Once the chemical potential touches either the conduction or the valence band edge, the double layer becomes charge-compressible; it screens out the AC electric field, and C_P drops to a small value. (The observed negative values arise from the electron correlation effects in the double layer [33] and the non-overlapped monolayer regions in the dual-gated device, Extended Data Fig. 1.) The gate voltage between the rising and falling edges of C_P provides an estimate of the band gap energy $E_G \approx 0.68$ eV (see Extended Data Fig. 2 for E_G as a function of Δ). Figure 1d also shows that the charge gap energy decreases as the bias voltage increases; the gap closes at $eV_b \approx E_G$. More rigorously, the charge gap energy can be evaluated by integrating C_P over the incompressible regime [33], $\Delta\mu \approx \int dV_g\,(C_P/C_{gg})$.

We simultaneously measure the exciton compressibility through the interlayer capacitance. We probe the differential charge density on one layer (W-layer) induced by an AC voltage dV_b applied to the other layer (Mo-layer) (Fig. 1e). The differential charge density, arising from transfer of a charge from one layer to the other, is also the differential exciton density, dn_X. The AC voltage dV_b modulates the exciton chemical potential [15, 16]. The interlayer capacitance per unit area, $C_I = e\frac{dn_X}{dV_b}$, thus directly measures the isothermal exciton compressibility $\kappa_X = \left(\frac{\partial n_X}{\partial \mu_X}\right)_T$. Figure 1f shows the bias dependence of C_I at equal electron and hole densities ($V_g \approx 0$ V). The interlayer capacitance rises abruptly from zero when V_b exceeds a threshold ($\approx E_G/e$). It decreases gradually and approaches the geometrical capacitance of the double layer, C_{2L}, with further increase of bias voltage. We determine the exciton density by integrating C_I with respect to the bias voltage, $n_X = \int dV_b \frac{C_I}{e}$ (red curve). An exciton density up to 10^{12} cm^{-2} can be achieved with a bias on the order of 1 V.

Electrostatics phase diagram

We analyze the double-layer device based on the parallel-plate capacitor model and known device parameters (Methods). The W-layer is grounded, as in the experiment. Figure 2a shows four doping regions for the double layer as a function of bias and gate voltages when electron-hole interactions are neglected. Here, *i*, *p* and *n* denote intrinsic,

positively doped, and negatively doped regions for each layer, respectively. Under small bias and gate voltages, both layers are intrinsic (the *ii*-region). The double layer enters the *pn*-region when V_b exceeds a threshold. The threshold is weakly dependent on V_g because with $C_{2L} \gg C_{gg}$, the bias voltage is much more efficient than the gate voltage in tuning the charge chemical potentials.

The capacitance measurements are in good agreement with the electrostatics simulation result: the area with large C_P ($\approx C_{gg}$, shown in red in Fig. 2b) corresponds to the *ii*-region, and the area with large C_I (also shown in red, Fig. 2c) corresponds to the *pn*-region. This agreement shows that the electron-hole fluid is in equilibrium with the electrodes, which provide an electrical reservoir for interlayer excitons. The conclusion is further supported by the long interlayer exciton lifetime (~ 1 ms), determined from an independent tunneling measurement (Extended Data Fig. 3).

Exciton insulator

In the absence of electron-hole interactions in the double layer, charge gap closing (at the tip of the red triangle in Fig. 2b) and electron-hole pair injection (emergence of C_I, the red region in Fig. 2c) are expected to occur at the same bias threshold that is defined by the band gap energy E_G. A careful examination reveals, however, that the bias threshold for pair injection (horizontal white line II) is about 25 mV lower than the threshold for band gap closing (horizontal white line I). There exists a finite range of the bias and gate voltages (enclosed by the red and white dashed lines), within which a charge gap and electrons/holes are both present. In this regime, the electron-hole fluid is a bosonic fluid of bound electron-hole pairs. It is an EI by definition and is expected to be a 2D superfluid at sufficiently low temperatures. The difference between the two bias thresholds also provides an estimate of the interlayer exciton binding energy $E_B \sim 25 \pm 5$ meV.

The charge-gap can be viewed as density-dependent E_B since it corresponds to the chemical potential jump from an exciton fluid with one extra electron to one with an extra hole [16], and is generally expected to vanish when a critical (Mott) density is reached [23]. Our ability to continuously vary the exciton density n_X in the double layer allows us to measure E_B as a function of n_X. We vary the exciton density by tuning V_b according to Fig. 1f. At each bias, we determine the charge gap energy $\Delta\mu$ from the gate dependence of the penetration capacitance (Extended Data Fig. 4). We use the charge gap at 15 K to approximate E_B. The binding energy decreases continuously as n_X increases (Fig. 3). The extrapolated value of E_B at zero density, 17.5 ± 2.5 meV, is consistent with our previous estimate and corresponds to an exciton Bohr radius of $a_B \sim 7$ nm. The binding energy drops to zero around $n_X \approx 8 \times 10^{11}$ cm^{-2} (the Mott density), above which the EI turns into an electron-hole plasma [23]. We obtain $n_X a_B^2 \sim 0.4$, which agrees reasonably well with the Mott density estimate $n_X a_B^2 \sim 0.3 - 0.7$ (Ref. [34, 35]). We do not observe any abrupt transition from the EI to a charge conductor around the Mott density down to 10-15 K, indicating the possibility of a continuous Mott transition.

The charge gap at a given exciton density also depends on temperature (Fig. 3). It decreases with increasing temperature and vanishes around T_s. Figure 4a shows T_s

(squares) as a function of exciton density. The trend is similar to the density dependence of E_B (15 K in Fig. 3). We find $k_B T_s$ (k_B denoting the Boltzmann constant) is about 40% of the exciton binding energy for the entire density range. The temperature T_s thus represents the ionization (or Saha) temperature of the exciton fluid [23]. Above T_s, a sizable portion of the excitons is ionized and the double layer becomes charge-compressible ($C_P \approx 0$).

Exciton phase diagram

Finally, we construct the density-temperature phase diagram of the excitons at equal electron and hole densities in Fig. 4a. The color represents the magnitude of the interlayer capacitance C_I, or equivalently, the exciton compressibility κ_X. The phase diagram consists of a dome of large κ_X (shown in red). The exciton ionization temperature T_s characterizes a crossover from an EI (left) to an electron-hole plasma (right). Figure 4b shows representative horizontal line cuts of Fig. 4a. At a given temperature, C_I increases linearly with density, reaches a peak, and gradually approaches the interlayer geometrical capacitance C_{2L}. As temperature increases, the peak shifts towards higher density while the peak amplitude decreases. We mark the peak location (T^{**}) with a dotted line in Fig. 4a. Generally, T^{**} is 5-6 times larger than the degeneracy temperature per flavor estimated for non-interacting bosons, $T^* = 2n_X/D$ (dashed line) [23], where $D = \frac{m}{\pi\hbar^2}$ is the 2D exciton density of states, defined by the exciton mass $m \approx m_0$ and the reduced Planck constant $\hbar$ (m_0 is the free electron mass).

The density dependence of the exciton compressibility indicates the importance of exciton-exciton interactions [15, 16, 24, 25, 36]. We consider an interacting Bose gas model with a coupling constant g (Ref. [24]) (gn_X describes the interaction energy per exciton). The mean-field isothermal compressibility is given by $\kappa_X = \frac{D}{gD+[\exp(n_X/DkT)-1]^{-1}}$ (Methods). The result reduces to a linear density dependence, $\kappa_X \approx n_X/(gn_X + k_B T)$, in the high-temperature (non-degenerate) limit, and a constant, $\kappa_X \approx g^{-1}$, in the low-temperature (degenerate) limit. We extract the dimensionless coupling constant, $gD \approx 11$, from analysis of κ_X in the non-degenerate limit (Extended Data Fig. 5), which is in good agreement with mean-field calculations for interacting bosons in TMD double layers [15, 16, 24]. The compressibility peak in Fig. 4b is, however, in contradiction to the assumption of a density-independent g. It suggests that g increases with density as the exciton wavefunctions start to overlap. The compressibility peak occurs when the interaction energy is comparable to the thermal excitation energy, $gn_X \sim k_B T^{**}$. The ratio of T^{**} and T^* therefore corresponds to $\sim gD/2 \sim 5-6$, consistent with the result from the non-degenerate limit.

The large dimensionless coupling constant gD shows that the exciton fluid is strongly correlated. The strong correlation suppresses exciton density fluctuations [9, 37]; it enhances the effective degeneracy temperature from T^* to $\sim T^{**}$ (Ref. [10]) that characterizes a crossover from a non-degenerate to a degenerate exciton fluid (often referred to as a quasi-condensate [9, 10, 37]). The strong correlation is also expected to suppress phase fluctuations and enhance the exciton superfluid transition temperature [9, 10, 37], below which quasi-long-range quantum coherence emerges. As density increases, the

phase diagram (Fig. 4a) is expected to exhibit a BEC-BCS crossover, which is complicated by the density-dependent screening effect of the electron-hole interaction in TMD double layers (BEC and BCS stand for Bose-Einstein condensation and Bardeen-Cooper-Schrieffer, respectively). Future exciton transport studies (e.g. by counter-flow measurements [38]) are required to unveil the excitonic superfluid transition and the BEC-BCS crossover.

References

1. Mott, N.F. The transition to the metallic state. *The Philosophical Magazine: A Journal of Theoretical Experimental and Applied Physics* **6**, 287-309 (1961).
2. Jérome, D., Rice, T.M. & Kohn, W. Excitonic Insulator. *Physical Review* **158**, 462-475 (1967).
3. Zhu, X., Littlewood, P.B., Hybertsen, M.S. & Rice, T.M. Exciton Condensate in Semiconductor Quantum Well Structures. *Physical Review Letters* **74**, 1633-1636 (1995).
4. Sun, Z. & Millis, A.J. Topological Charge Pumping in Excitonic Insulators. *Physical Review Letters* **126**, 027601 (2021).
5. Eisenstein, J.P. & MacDonald, A.H. Bose–Einstein condensation of excitons in bilayer electron systems. *Nature* **432**, 691-694 (2004).
6. Kogar, A., Rak, M.S., Vig, S., Husain, A.A., Flicker, F., Joe, Y.I., Venema, L., MacDougall, G.J., Chiang, T.C., Fradkin, E., van Wezel, J. & Abbamonte, P. Signatures of exciton condensation in a transition metal dichalcogenide. *Science* **358**, 1314 (2017).
7. Butov, L.V. Condensation and pattern formation in cold exciton gases in coupled quantum wells. *Journal of Physics: Condensed Matter* **16**, R1577-R1613 (2004).
8. Baranov, M.A., Dalmonte, M., Pupillo, G. & Zoller, P. Condensed Matter Theory of Dipolar Quantum Gases. *Chemical Reviews* **112**, 5012-5061 (2012).
9. Z. Hadzibabic & Dalibard, J. Two-dimensional Bose fluids: An atomic physics perspective. *Rivista del Nuovo Cimento* **34**, 389 (2011).
10. Lozovik, Y.E., Kurbakov, I.L., Astrakharchik, G.E., Boronat, J. & Willander, M. Strong correlation effects in 2D Bose–Einstein condensed dipolar excitons. *Solid State Communications* **144**, 399-404 (2007).
11. Ha, L.-C., Hung, C.-L., Zhang, X., Eismann, U., Tung, S.-K. & Chin, C. Strongly Interacting Two-Dimensional Bose Gases. *Physical Review Letters* **110**, 145302 (2013).
12. Cercellier, H., Monney, C., Clerc, F., Battaglia, C., Despont, L., Garnier, M.G., Beck, H., Aebi, P., Patthey, L., Berger, H. & Forró, L. Evidence for an Excitonic Insulator Phase in 1T-TiSe2. *Physical Review Letters* **99**, 146403 (2007).
13. Seki, K., Wakisaka, Y., Kaneko, T., Toriyama, T., Konishi, T., Sudayama, T., Saini, N.L., Arita, M., Namatame, H., Taniguchi, M., Katayama, N., Nohara, M., Takagi, H., Mizokawa, T. & Ohta, Y. Excitonic Bose-Einstein condensation in Ta2NiSe5. *Physical Review B* **90**, 155116 (2014).
14. Du, L., Li, X., Lou, W., Sullivan, G., Chang, K., Kono, J. & Du, R.-R. Evidence for a topological excitonic insulator in InAs/GaSb bilayers. *Nature Communications* **8**, 1971 (2017).

15. Xie, M. & MacDonald, A.H. Electrical Reservoirs for Bilayer Excitons. *Physical Review Letters* **121**, 067702 (2018).
16. Zeng, Y. & MacDonald, A.H. Electrically controlled two-dimensional electron-hole fluids. *Physical Review B* **102**, 085154 (2020).
17. Burg, G.W., Prasad, N., Kim, K., Taniguchi, T., Watanabe, K., MacDonald, A.H., Register, L.F. & Tutuc, E. Strongly Enhanced Tunneling at Total Charge Neutrality in Double-Bilayer Graphene-WSe2 Heterostructures. *Physical Review Letters* **120**, 177702 (2018).
18. Su, J.-J. & MacDonald, A.H. How to make a bilayer exciton condensate flow. *Nature Physics* **4**, 799-802 (2008).
19. Yu. E. Lozovik & Yudson, V.I. A new mechanism for superconductivity: pairing between spatially separated electrons and holes. *Zh. Eksp. Teor. Fiz.* **71**, 738-753 (1976).
20. Dolcini, F., Rainis, D., Taddei, F., Polini, M., Fazio, R. & MacDonald, A.H. Blockade and Counterflow Supercurrent in Exciton-Condensate Josephson Junctions. *Physical Review Letters* **104**, 027004 (2010).
21. Halperin, B.I. & Rice, T.M. Possible Anomalies at a Semimetal-Semiconductor Transistion. *Reviews of Modern Physics* **40**, 755-766 (1968).
22. Kohn, W. & Sherrington, D. Two Kinds of Bosons and Bose Condensates. *Reviews of Modern Physics* **42**, 1-11 (1970).
23. Fogler, M.M., Butov, L.V. & Novoselov, K.S. High-temperature superfluidity with indirect excitons in van der Waals heterostructures. *Nature Communications* **5**, 4555 (2014).
24. Wu, F.-C., Xue, F. & MacDonald, A.H. Theory of two-dimensional spatially indirect equilibrium exciton condensates. *Physical Review B* **92**, 165121 (2015).
25. Skinner, B., Yu, G.L., Kretinin, A.V., Geim, A.K., Novoselov, K.S. & Shklovskii, B.I. Effect of dielectric response on the quantum capacitance of graphene in a strong magnetic field. *Physical Review B* **88**, 155417 (2013).
26. Zhiyuan Sun, Tatsuya Kaneko, Denis Golež & Millis, A.J. Second order Josephson effect in excitonic insulators. *arXiv:2102.10455* (2021).
27. Wang, Z., Rhodes, D.A., Watanabe, K., Taniguchi, T., Hone, J.C., Shan, J. & Mak, K.F. Evidence of high-temperature exciton condensation in two-dimensional atomic double layers. *Nature* **574**, 76-80 (2019).
28. Jauregui, L.A., Joe, A.Y., Pistunova, K., Wild, D.S., High, A.A., Zhou, Y., Scuri, G., De Greve, K., Sushko, A., Yu, C.-H., Taniguchi, T., Watanabe, K., Needleman, D.J., Lukin, M.D., Park, H. & Kim, P. Electrical control of interlayer exciton dynamics in atomically thin heterostructures. *Science* **366**, 870 (2019).
29. Paik, E.Y., Zhang, L., Burg, G.W., Gogna, R., Tutuc, E. & Deng, H. Interlayer exciton laser of extended spatial coherence in atomically thin heterostructures. *Nature* **576**, 80-84 (2019).
30. Li, J.I.A., Taniguchi, T., Watanabe, K., Hone, J. & Dean, C.R. Excitonic superfluid phase in double bilayer graphene. *Nature Physics* **13**, 751-755 (2017).
31. Liu, X., Watanabe, K., Taniguchi, T., Halperin, B.I. & Kim, P. Quantum Hall drag of exciton condensate in graphene. *Nature Physics* **13**, 746-750 (2017).

32. Rivera, P., Yu, H., Seyler, K.L., Wilson, N.P., Yao, W. & Xu, X. Interlayer valley excitons in heterobilayers of transition metal dichalcogenides. *Nature Nanotechnology* **13**, 1004-1015 (2018).
33. Eisenstein, J.P., Pfeiffer, L.N. & West, K.W. Negative compressibility of interacting two-dimensional electron and quasiparticle gases. *Physical Review Letters* **68**, 674-677 (1992).
34. De Palo, S., Rapisarda, F. & Senatore, G. Excitonic Condensation in a Symmetric Electron-Hole Bilayer. *Physical Review Letters* **88**, 206401 (2002).
35. López Ríos, P., Perali, A., Needs, R.J. & Neilson, D. Evidence from Quantum Monte Carlo Simulations of Large-Gap Superfluidity and BCS-BEC Crossover in Double Electron-Hole Layers. *Physical Review Letters* **120**, 177701 (2018).
36. Skinner, B. & Shklovskii, B.I. Anomalously large capacitance of a plane capacitor with a two-dimensional electron gas. *Physical Review B* **82**, 155111 (2010).
37. Kagan, Y., Kashurnikov, V.A., Krasavin, A.V., Prokof'ev, N.V. & Svistunov, B.V. Quasicondensation in a two-dimensional interacting Bose gas. *Physical Review A* **61**, 043608 (2000).
38. Xiaomeng Liu, J.I.A. Li, Kenji Watanabe, Takashi Taniguchi, James Hone, Bertrand I. Halperin, Philip Kim & Dean, C.R. Crossover between Strongly-coupled and Weakly-coupled Exciton Superfluids. *arXiv:2012.05916* (2020).

Figure legends

Figure 1 | Electrical reservoir for interlayer excitons. a, Type II band alignment of $MoSe_2/WSe_2$ double layers with interlayer band gap E_G (left). A bias voltage V_b across the layers separates the electron and hole chemical potentials (dashed lines) and reduces the charge gap (right). Interlayer excitons are formed spontaneously when the bias voltage, which acts as a chemical potential for excitons, exceeds the exciton energy $E_G - E_B$. **b,** Schematic cross-section of dual-gated double layer devices. The anti-symmetric gating Δ reduces E_G in the region of interest; it closes E_G in the contact region to heavily dope the TMDs. The symmetric gating V_g shifts the electron and hole chemical potentials together and tune their density difference. **c, e,** Schematics of the penetration (**c**) and interlayer capacitance (**e**) measurements. The double layer is AC grounded in **c**. **d,** Gate dependence of the normalized penetration capacitance at representative bias voltages. The sharp capacitance drops signify electron or hole doping into the double layer. The charge gap is closed for $V_b \approx 0.7$ V. **f,** Bias dependence of the normalized interlayer capacitance (black) and the exciton density (red) at $V_g = 0$. **d** and **f** are measured at 15 K and $\Delta = 4.6$ V.

Figure 2 | Exciton and charge compressibility. a, Electrostatics simulation of double layer Device 1 based on the parallel-plate capacitor model. The electron-hole interaction is ignored. The double layer can be in one of the four doping regions as a function of bias and gate voltages (*i*, *p* and *n* denoting an intrinsic, positively and negatively doped layer). The *ii* region (white) is enclosed by a vertical line (valence band edge of the grounded W-layer) and a line of slope -1 (conduction band edge of the Mo-layer). **b, c,** Normalized penetration capacitance C_P/C_{gg} (**b**) and interlayer capacitance C_I/C_{2L} (**c**) as a function of bias and gate voltages, where C_{gg} and C_{2L} are the gate-to-gate and interlayer geometrical

capacitances, respectively. The charge incompressible region in **b** is enclosed by red dashed lines. White dashed line I and II correspond to the bias voltages at which the charge gap closes and the exciton population appears, respectively. Their difference (25 mV) provides an estimate of the exciton binding energy in the limit of zero density. The measurements are performed at 15 K and $\Delta = 4.6$ V.

Figure 3 | Charge gap energy of the double layer. The charge gap energy as a function of exciton density at different temperatures (symbols). Each data point is extracted from the gate dependence of the penetration capacitance for a fixed bias voltage and temperature. The error bar shows the typical uncertainty of the analysis as described in Extended Data Figure 4. The lines are a guide to the eye.

Figure 4 | Exciton phase diagram. a, Normalized interlayer capacitance, or equivalently, exciton compressibility as a function of temperature and exciton density. The white squares denote the exciton ionization temperature T_s, which characterizes a crossover from the EI (left) to an electron-hole plasma (right). The error bar shows the typical uncertainty of the analysis as described in Extended Data Figure 4. The dashed line T^* and dotted line T^{**} show, respectively, the degeneracy temperature per flavor for non-interacting excitons and the temperature corresponding to the exciton compressibility peak. The error bar represents the typical uncertainty in density of the compressibility peak. **b,** Exciton compressibility as a function of exciton density at varying temperatures. The compressibility peak divides the high-temperature (left) and low-temperature (right) regime.

Methods

Device design and fabrication

A schematic of the dual-gated $MoSe_2$/hBN/WSe_2 devices is shown in Fig. 1b. The top and bottom gates consist of hBN gate dielectrics of 10 - 20 nm in thickness and few-layer graphite gate electrodes. The two gates are typically symmetric. The hBN spacer between the two TMD monolayers has a different thickness in the region of interest (~ 1.5 - 2 nm) and in the contact region (10 - 20 nm). This is crucial to achieve good metal-TMD contacts as discussed below. The design allows us to achieve equilibrium exciton fluids by biasing the two TMD monolayers at ~ 1 V. Before the charge gap is closed, the tunneling current is negligible (Extended Data Fig. 3) and the exciton density is fully determined by the electrostatics (Fig. 2).

This is in contrast to the previously reported devices [27]. There, excitons can be injected only under high bias (~ 5 - 6 V) because there is a large Schottky barrier at the graphite-TMD contacts and a significant portion of the bias voltage drops at the contact [16]. The electron/hole layer cannot be maintained at the same chemical potential as the contacts. The electrical contact resistances dominate the tunnel junction resistance; and the devices are in the small tunnel junction resistance regime. A large tunneling current accompanies the injection of excitons. The exciton density is determined by balancing the pumping and recombination rates of excitons [16]. They are non-equilibrium exciton fluids.

The current design circumvents the electrical contact issue by combining several strategies. We use Pt instead of graphite as contact electrodes; Pt has been reported to form good contacts to both $MoSe_2$ and WSe_2 monolayers [39, 40]. We heavily dope the TMDs in the contact region (but not in the region of interest) to form good metal-TMD contacts. This is achieved by applying a large vertical electric field (from anti-symmetric gating). The field creates a vertical voltage drop between the two TMD layers that is linearly proportional to the layer separation. We design a substantially thicker hBN spacer in the contact region than in the region of interest so that the interlayer band gap is closed in the contact region while it is only reduced in the region of interest. In addition, to further suppress electron tunneling between the TMD layers, we increase the thickness of the hBN spacer in the region of interest from 2-3 layers as in the reported devices [27] to 5-6 layers. Our devices are in the large tunnel junction resistance regime. We also find that it is crucial to have the electron and hole contacts close by to inject bound pairs at low temperatures. Extended Data Fig. 7 shows an example in which the electron and hole contacts are not close by. Injection of excitons is through a thermally assisted process.

We fabricate the devices using the reported dry transfer technique [41]. The constituent layers are exfoliated from bulk TMD crystals (HQ Graphene) and other crystals onto Si substrates covered by a 285 nm-thick SiO_2 layer. Their thickness is first identified by optical reflection microscopy and subsequently confirmed by atomic force microscopy (AFM). The layers are picked up from substrates consecutively at ~ 50°C using a polymer stamp made of a thin layer of polycarbonate on a polypropylene-carbonate-coated polydimethylsiloxane block. The complete stack is then released onto an amorphous quartz substrate with pre-patterned Pt electrodes at 200°C. The residual polycarbonate film is removed in chloroform and isopropanol. Amorphous quartz is chosen as substrates for minimal parasitic capacitance background. The background is also temperature independent, which allows capacitance studies over a broad temperature range. We have examined multiple devices in this study. The results are highly reproducible. Extended Data Figure 1 shows the optical image of Device 1 and 2. The results in the main text are from Device 1. The main results from Device 2 and 3 are shown in Extended Data Fig. 6 and 7, respectively.

Choice of the TMD compounds

In principle, any TMD heterobilayers that have a type II band alignment can be used to create a strongly correlated exciton fluid. Examples include $MoSe_2/WSe_2$, MoS_2/WSe_2 and WSe_2/WS_2 (Ref. [42]). In Extended Data Fig. 7 we show results from a MoS_2/WSe_2 heterobilayer device with the electron and hole contacts not close by. There are, however, several practical considerations in the selection of the TMD compounds. The first is formation of good electrical contacts, which is currently limited to TMDs such as MoS_2, $MoSe_2$, $MoTe_2$ and WSe_2. The second is good material quality. $MoSe_2$ and WSe_2 tend to have higher charge carrier mobilities and less disorder densities compared to the others. The third is chemical stability. Sulfide- and selenide-based TMDs are generally air stable and easier to handle.

Capacitance measurements

We perform two types of capacitance measurements. The first is the penetration capacitance. We apply a small AC voltage dV_{tg} of root mean square (rms) amplitude 5 mV and frequency 423 Hz to the top gate. It generates an AC electric field that can penetrate the AC-grounded TMD double layer and induce a small charge density dn_{bg} on the bottom gate. The induced charge density is measured using a low-temperature integrated capacitance bridge based on a GaAs high-electron-mobility transistor (HEMT) amplifier [43]. The measurement circuit diagram is shown in Extended Data Fig. 8a. The AC voltage dV_{tg} modulates both the charge carrier density dn and the chemical potential $d\mu$ of the entire double layer. Using an equivalent circuit model for the device (Extended Data Fig. 8b) and ignoring a small contribution from the layer polarizability of the double layer [44], we derive the penetration capacitance, $C_P = e\frac{dn_{bg}}{dV_{tg}} \approx \frac{C_{gg}^2}{C_Q/4+C_{gg}}$, where $C_Q = e^2 dn/d\mu$ is the junction's quantum capacitance, and C_{gg} is the gate-to-gate geometrical capacitance per unit area. The measured C_P is independent of frequency ranging from 77 Hz to 3.3 kHz.

We also measure the interlayer capacitance (the capacitance of the $MoSe_2$/hBN/WSe_2 junctions). The equivalent circuit consists of an interlayer capacitance and a tunneling resistance in parallel. For each DC bias voltage and gate voltage, we apply a small AC excitation voltage dV_b (rms amplitude 5 mV and frequency f = 1187 Hz) to the Mo-layer, and detect the induced interlayer current dI from the W-layer. The interlayer current is complex in general. The in-phase component $dI^{(1)}$ corresponds to the interlayer tunneling current; and the out-of-phase component, the displacement current $dI^{(2)}$, is proportional to the change in exciton density dn_X. Both in-phase and out-of-phase components (after a preamplifier) are detected with a lock-in amplifier (SR830). The interlayer capacitance reported in the main text is defined by the displacement current, $C_I = \frac{1}{2\pi f A}\frac{dI^{(2)}}{dV_b}$, where $A \approx 34$ μm^2 is the area of the double layer region. The measurement results are independent of the excitation amplitude (2 - 15 mV) and frequency (77 Hz to 7.7 kHz).

Interlayer band gap

The interlayer band gap E_G of the TMD double layer is controlled by anti-symmetric gating $\Delta \equiv (V_{bg} - V_{tg})/2$. It creates an out-of-plane electric field and a voltage drop of $\approx \frac{t_{2L}}{t_{gg}} 2\Delta$ between the TMD layers from geometrical considerations. Here t_{2L} and t_{gg} are the TMD interlayer separation and the gate-to-gate separation, respectively. The voltage drop reduces the interlayer band gap linearly, $E_G \approx E_G^0 - \frac{t_{2L}}{t_{gg}} 2e\Delta$, where E_G^0 is the intrinsic gap value. As described in the main text, the interlayer band gap can be measured from the penetration capacitance under zero bias; it corresponds to the voltage separation between the capacitance rising and falling edges (Fig. 1d). Extended Data Fig. 2 shows the measured gap as a function of anti-symmetric gating Δ. It is well described by a linear dependence with a slope of about $0.21e$. This is fully consistent with the geometry of the device $2\frac{t_{2L}}{t_{gg}} \approx 2\frac{2\ nm}{20\ nm} \approx 0.2$. The extrapolated gap at zero bias (1.6 eV) is also in good agreement with the reported interlayer band gap (under zero electric field) for

$MoSe_2/WSe_2$ double layers [45]. All the data presented in the main text were taken at $\Delta = 4.6$ V, which corresponds to $E_G \approx 0.68$ eV.

Electrostatics simulation

We can model the electrostatics of the devices approximately using the parallel-plate capacitor model (Extended Data Fig. 9) that neglects the exciton binding energy. We express the electron density ($n_e > 0$) in the Mo-layer and the hole density ($n_h > 0$) in the W-layer for given bias voltage V_b and gate voltages V_{tg} and V_{bg} as

$$n_e e^2 \approx 2C_{gg}\left(eV_{bg} - \phi_M\right) + C_{2L}(\phi_W - \phi_M), \quad (1)$$

$$n_h e^2 \approx 2C_{gg}\left(\phi_W - eV_{tg}\right) + C_{2L}(\phi_W - \phi_M). \quad (2)$$

Here $\phi_M = \mu_e - eV_b$ and $\phi_W = -\mu_h$ are the electrostatic potential of the Mo- and W-layer, respectively; $\mu_e > 0$ and $\mu_h > 0$ are the electron and hole chemical potentials, respectively; C_{gg} and C_{2L} are the gate-to-gate and the TMD double layer geometrical capacitance per unit area, respectively. We can relate the chemical potentials to the carrier densities through the electronic density of states, $\mu_e = \frac{E_G}{2} + \frac{\pi\hbar^2}{m_e} n_e$ and $\mu_h = \frac{E_G}{2} + \frac{\pi\hbar^2}{m_h} n_h$. Here $m_e \approx m_h (\approx 0.5 m_0)$ [46] are the electron and hole band masses (m_0 denoting the free electron mass) and $\hbar$ is the reduced Planck constant. We solve equations (1) and (2) for n_e and n_h.

The result in Fig. 2a is obtained for Device 1 using the experimentally calibrated geometrical capacitances, $C_{gg} = (1.53 \pm 0.05) \times 10^{-7}$ Fcm^{-2} and $C_{2L} = (14.9 \pm 0.3) \times 10^{-7}$ Fcm^{-2}. These values are consistent with the result of the parallel-plate capacitor model using the known device parameters, $C_{gg} = \frac{\epsilon_0}{(2t_g/\epsilon_{BN} + t_{2L}/\epsilon_{BN} + t_M/\epsilon_M + t_W/\epsilon_W)} \approx \frac{\epsilon_{BN}\epsilon_0}{2t_g + t_{2L}} \approx 1.41 \times 10^{-7}$ Fcm^{-2} and $C_{2L} = \frac{\epsilon_0}{(t_{2L}/\epsilon_{BN} + t_M/2\epsilon_M + t_W/2\epsilon_W)} \approx \frac{\epsilon_{BN}\epsilon_0}{t_{2L}} \approx 15.5 \times 10^{-7}$ Fcm^{-2}. Here $t_g \approx 10$ nm and $t_M \approx t_W \approx 0.65$ nm denote the sample-to-gate distance and the thickness of the Mo- and W-layer, respectively; $\epsilon_{BN} \approx 3.5$ (Ref. [39]) and $\epsilon_M \approx \epsilon_W \approx 7$ (Ref. [47]) are the dielectric constant of hBN and of $MoSe_2$ and WSe_2, respectively; (ϵ_0 is the vacuum permittivity).

Interlayer tunneling current and exciton lifetime

In addition to the interlayer capacitance, we monitor the DC tunneling current I in the double layer. Extended Data Fig. 3a shows the tunneling current as a function of bias voltage V_b with equal electron and hole densities. The different curves correspond to different anti-symmetric gating Δ, which varies the interlayer band gap energy E_G. The current onset is observed approximately when $eV_b \gtrsim E_G$.

The different regimes of tunneling are illustrated in Extended Data Fig. 3b for a fixed anti-symmetric gating Δ= 4.3 V. The tunneling current remains relatively small over an extended range of bias voltage above the threshold (~ 1 nA or smaller, corresponding to a tunneling current density of no more than 0.03 nA/μm^2). The tunneling current density is over four orders of magnitude smaller than that in the devices reported in Ref. [27].

Tunneling in this regime arises from a non-resonant process (left inset). We focus on the equilibrium regime ($V_b < 1.7$ V) in this study. In this regime, the exciton lifetime, τ_X, can be estimated from the tunneling current density and the exciton density: $\tau_X \approx \frac{eAn_X}{I}$. Extended Data Figure 3c shows the bias dependence of τ_X. The exciton lifetime is on the order of millisecond.

When V_b exceeds ~ 1.7 V (independent of Δ), the tunneling current increases dramatically. The value agrees well with the band gap of monolayer $MoSe_2$ (Ref. [45]). In this regime, tunneling arises from a resonant process (right inset, Extended Data Fig. 3b) and strong intralayer exciton electroluminescence is observed (Extended Data Fig. 3d). A non-equilibrium exciton fluid is formed. The exciton density is determined by balancing the pumping and recombination rates, rather than by electrostatics, as studied in Ref. [27].

Compressibility of a 2D interacting Bose gas

The density of a 2D interacting Bose gas is related to the Bose-Einstein statistics as

$$n_X = \int_0^\infty d\epsilon_X \frac{D}{\exp[(\epsilon_X + gn_X - \mu_X)/k_BT] - 1} = -DT \times \ln[1 - \exp\left(\frac{\mu_X - gn_X}{k_BT}\right)]. \quad (3)$$

Here $D = \frac{m}{\pi\hbar^2}$ is the exciton density of states in 2D with exciton mass $m = m_e + m_h$, ϵ_X and μ_X are the exciton kinetic energy and chemical potential, respectively, and g is the exciton-exciton coupling constant. The mean-field isothermal exciton compressibility is evaluated as $\kappa_X = \left(\frac{\partial n_X}{\partial \mu_X}\right)_T$.

We evaluate the coupling constant g by analyzing the compressibility in the high-temperature limit. Extended Data Figure 5 shows the temperature dependence of the inverse interlayer capacitance (symbols) at representative densities in this regime. The data are well described by the mean-field result (solid lines), $C_I^{-1} \propto \kappa_X^{-1} \approx g + \frac{k_B}{n_X}T$. The *y*-intercept is proportional to g, and the *x*-intercept is given by $-gn_X/k_B$. Extended Data Figure 5b shows the magnitude of the *x*-intercept as a function of density. We extract $g \approx (2.6 \pm 0.1) \times 10^{-14}$ eVcm^2 (corresponding to $gD \approx 11$) from the slope of the linear fit (solid line). A similar value is also obtained from the *y*-intercept and the known device area of A. The positive sign of g indicates a repulsive interaction. The g value is also in good agreement with a mean-field calculation for interacting bosons in TMD double layers ($g = 3 \times 10^{-14}$ eVcm^2) [24].

We can also extract the entropy change per exciton, $\left(\frac{\partial S}{\partial n_X}\right)_T$, at a given temperature (Extended Data Fig. 10) from the temperature dependence of the chemical potential, $\mu_X(T)$, using the Maxwell's relation, $\left(\frac{\partial \mu_X}{\partial T}\right)_{n_X} = -\left(\frac{\partial S}{\partial n_X}\right)_T$. Here S denotes the 2D entropy density. The exciton chemical potential is extracted from the measured compressibility. Extended Data Fig. 10a shows the density dependence of the chemical potential $\mu_X(n_X)$ at varying temperatures T. Extended Data Fig. 10b replots μ_X as a function of T at varying exciton densities n_X. The chemical potential μ_X decreases

monotonically with temperature. We first fit the smooth dependence using a polynomial and then compute the derivative $\left(\frac{\partial \mu_X}{\partial T}\right)_{n_X}$.

As exciton density increases, the entropy change per exciton first drops rapidly then decreases slowly. The crossover is correlated with the compressibility peak in Fig. 4b. The substantially smaller entropy change per exciton at high densities is consistent with adding excitons mostly to the ground state. No thermodynamic signature of the 2D superfluid transition is observed as expected [48]. We also observe a broad entropy peak near the Mott density. It is related to the presence of a Mott critical point at zero temperature. Since the lowest measurement temperature is 10 K in this study, we are not able to access the Mott critical point; we only capture the broad entropy peak for the crossover at high temperatures.

Method references

39. Fallahazad, B., Movva, H.C.P., Kim, K., Larentis, S., Taniguchi, T., Watanabe, K., Banerjee, S.K. & Tutuc, E. Shubnikov--de Haas Oscillations of High-Mobility Holes in Monolayer and Bilayer WSe2: Landau Level Degeneracy, Effective Mass, and Negative Compressibility. *Physical Review Letters* **116**, 086601 (2016).
40. Larentis, S., Movva, H.C.P., Fallahazad, B., Kim, K., Behroozi, A., Taniguchi, T., Watanabe, K., Banerjee, S.K. & Tutuc, E. Large effective mass and interaction-enhanced Zeeman splitting of K-valley electrons in MoSe2. *Physical Review B* **97**, 201407 (2018).
41. Wang, L., Meric, I., Huang, P.Y., Gao, Q., Gao, Y., Tran, H., Taniguchi, T., Watanabe, K., Campos, L.M., Muller, D.A., Guo, J., Kim, P., Hone, J., Shepard, K.L. & Dean, C.R. One-Dimensional Electrical Contact to a Two-Dimensional Material. *Science* **342**, 614 (2013).
42. Gong, C., Zhang, H., Wang, W., Colombo, L., Wallace, R.M. & Cho, K. Band alignment of two-dimensional transition metal dichalcogenides: Application in tunnel field effect transistors. *Applied Physics Letters* **103**, 053513 (2013).
43. Ashoori, R.C., Stormer, H.L., Weiner, J.S., Pfeiffer, L.N., Pearton, S.J., Baldwin, K.W. & West, K.W. Single-electron capacitance spectroscopy of discrete quantum levels. *Physical Review Letters* **68**, 3088-3091 (1992).
44. Young, A.F. & Levitov, L.S. Capacitance of graphene bilayer as a probe of layer-specific properties. *Physical Review B* **84**, 085441 (2011).
45. Wilson, N.R., Nguyen, P.V., Seyler, K., Rivera, P., Marsden, A.J., Laker, Z.P.L., Constantinescu, G.C., Kandyba, V., Barinov, A., Hine, N.D.M., Xu, X. & Cobden, D.H. Determination of band offsets, hybridization, and exciton binding in 2D semiconductor heterostructures. *Science Advances* **3**, e1601832 (2017).
46. Mak, K.F. & Shan, J. Photonics and optoelectronics of 2D semiconductor transition metal dichalcogenides. *Nature Photonics* **10**, 216-226 (2016).
47. Kim, K., Larentis, S., Fallahazad, B., Lee, K., Xue, J., Dillen, D.C., Corbet, C.M. & Tutuc, E. Band Alignment in WSe2–Graphene Heterostructures. *ACS Nano* **9**, 4527-4532 (2015).

48. Kosterlitz, J.M. & Thouless, D.J. Ordering, metastability and phase transitions in two-dimensional systems. *Journal of Physics C: Solid State Physics* **6**, 1181-1203 (1973).

Acknowledgements
We thank Erich J. Mueller and Cory Dean for fruitful discussions. Research was supported by the U.S. Department of Energy (DOE), Office of Science, Basic Energy Sciences (BES), under Award # DE-SC0019481 (device fabrication and theoretical analysis) and DE-SC0022058 (optical characterization), the US Office of Naval Research under award number N00014-21-1-2471 (data analysis) and the National Science Foundation (NSF) under DMR-2004451 (capacitance measurement). Growth of the hBN crystals was supported by the Elemental Strategy Initiative of MEXT, Japan and CREST (JPMJCR15F3), JST. This work was performed in part at the Cornell NanoScale Facility, an NNCI member supported by NSF Grant NNCI-2025233. K.F.M. acknowledges support from the David and Lucille Packard Fellowship.

Author contributions
L.M. and P.X.N. fabricated the devices, performed the measurements and analyzed the data. Z.W. provided assistance in device fabrication. Y.Z. and A.H.M. provided theoretical support for the measurements. K.W. and T.T. grew the bulk hBN crystals. L.M., P.X.N., K.F.M. and J.S. designed the scientific objectives; K.F.M. and J.S. oversaw the project. All authors discussed the results and commented on the manuscript.

Author information
Supplementary Information is available for this paper.
Reprints and permission information is available online at www.nature.com/reprints.
Competing interests The authors declare no competing financial interests.
Correspondence and requests for materials should be addressed to J.S. or K.F.M.

Data availability
The source data that support the findings of this study are available with the paper.

Extended data figure legends
Extended Data Figure 1 | Optical image of Device 1 and 2. Schematic cross-section (upper panel) and optical micrograph (lower panel) of Device 1 (**a**) and Device 2 (**b**). Constituent layers in the stack include WSe_2 monolayer (red line), $MoSe_2$ monolayer (yellow line), top gate (TG, white dashed line), bottom gate (BG, white dashdotted line) and local gate (LG Mo, white dotted line). The region of interest is shaded brown ('1'). In Device 1, the TMD double layers are separated by a thick hBN spacer (blue line) in the contact region ('2'); the thin hBN spacer in the region of interest is not marked. Both

electrons and holes are injected into '1' from '2' through one edge (solid black line). In Device 2, electrons and holes are injected into '1' from the two long sides separately. The local gate is not shown in the schematics; it heavily dopes the isolated $MoSe_2$ region to form good contact to the metal electrode. The rectangular yellow bars are Pt electrodes. The scale bar is 5 μm.

Extended Data Figure 2 | Dependence of interlayer band gap on anti-symmetric gating. a, Gate dependence of penetration capacitance at 15 K under varying anti-symmetric gating Δ and $V_b = 0$ V. The step falls signify electron doping into the $MoSe_2$ conduction band (CB) or hole doping into the WSe_2 valence band (VB). The separation between the rising and falling edges determines the band gap E_G. An additional (small) step on the electron-doping side arises from the presence of a small non-overlapped $MoSe_2$ monolayer inside the dual-gated device that affects the penetration capacitance. **b,** Interlayer band gap E_G (symbols) extracted from **a** as a function of Δ. The linear fit (dashed line) has a slope of ~ $0.21e$. The gap energy extrapolated for Δ = 0 corresponds to the intrinsic band gap energy $E_G^0 \approx 1.6$ eV.

Extended Data Figure 3 | Tunneling current, exciton lifetime and electroluminescence (EL). a, Bias dependence of interlayer tunneling current of Device 1 under anti-symmetric gating $\Delta = 4.6$ V (red), 4.25 V (blue), 4.00 V (black), and 3.75 V (green). The current onset is observed approximately when $eV_b \gtrsim E_G$. **b,** Interlayer tunneling current over a large bias range at Δ = 4.3 V. The insets illustrate the non-resonant (left) and resonant (right) tunneling regimes. **c,** Estimated exciton lifetime as a function of V_b from the tunneling data at $\Delta = 4.6$ V in **a**. **d,** Bias dependence of the EL spectrum (upper) and spectrally integrated EL intensity (lower). The data are acquired simultaneously with the tunneling current in **b** at equal electron and hole densities at 30 K. The EL at 1.60-1.65 eV arises from intralayer exciton emission in $MoSe_2$; the feature below 1.60 eV is likely originated from impurity bound states. Intralayer exciton emission from WSe_2 is not observed presumably due to quenching from resonant energy transfer. The EL starts to emerge at bias voltages ~ 1.7 V (red dashed line), when the device enters the resonant tunneling regime. Both the tunneling current and the EL intensity increases drastically above 1.7 V.

Extended Data Figure 4 | Determination of the charge gap. The penetration capacitance (**a**) and the charge chemical potential of the double layer (**b**) at 15 K as a function of V_g at varying exciton densities. The capacitance peak shows the presence of a charge-incompressible state. The integrated area of the peak gives the chemical potential jump (or the charge gap) at equal electron-hole density. The zero point of the chemical potential shift in **b** has been shifted to V_g = 0 V for comparison of different exciton densities. The charge gap closes near the Mott density. **c, d,** Similar to **a, b,** at fixed exciton density $n_X = 2.4 \times 10^{11}$ cm^{-2} for different temperatures. The charge gap closes at the ionization temperature.

Extended Data Figure 5 | Exciton compressibility in the high-temperature limit. a, Inverse interlayer capacitance (or exciton compressibility) as a function of temperature at varying exciton densities. The lines are linear fits in the high-temperature limit, i.e.

$gn_X/k_B \lesssim T \lesssim T_S$. **b,** Amplitude of the extracted x-intercept in **a** as a function of exciton density. A linear fit (blue) gives $g = (2.6 \pm 0.1) \times 10^{-14}$ eVcm^2. The inset shows the density dependence of the slope extracted from **a** (symbols). The red line is the mean-field result described in the main text. The density range is the same as in the main panel. The vertical error bars are the uncertainty of the linear fit in **a**. The horizontal error bar is the typical uncertainty of the exciton density from the analysis shown in Fig. 1f.

Extended Data Figure 6 | Main results from Device 2. Normalized penetration capacitance **(a)** and interlayer capacitance **(b)** as a function of bias and gate voltages at 20 K. The Mo-layer is grounded and the bias voltage is applied to the W-layer. The two red dashed lines denote the conduction band edge of $MoSe_2$ (vertical line) and the valence band edge of WSe_2 (line with slope +1). The contour plot is flipped horizontally compared to Fig. 2 of the main text for Device 1, in which the W-layer is grounded and the bias voltage is applied to the Mo-layer. There the valence band edge of WSe_2 corresponds a vertical line, and the conduction band edge of $MoSe_2$, a line with slope -1. The two white dashed lines denote the bias voltage at which the charge gap closes (I) and the exciton fluid becomes compressible (II). The difference between the two values (~ 40 mV) corresponds to the exciton binding energy in the limit of zero exciton density. The exciton binding energy in Device 2 with a slightly thinner hBN spacer (~ 5-layer) is larger than that in Device 1 (~ 25 mV).

Extended Data Figure 7 | Penetration and interlayer capacitances of Device 3. a,b, Penetration capacitance C_P (**a**) and interlayer capacitance C_I (**b**) as a function of bias and gate voltages at 10 K. The device is a MoS_2/WSe_2 double layer with the electron and hole contacts not close by. The Mo-layer is grounded. The two red dashed lines denote the conduction band edge of MoS_2 (vertical line) and the valence band edge of WSe_2 (line with slope +1). The charge incompressible region is enclosed by red dashed lines. White dashed lines correspond to the bias voltages at which the charge gap closes and the exciton population is expected to appear, respectively. Exciton injection without creating free charges is not observed, corresponding to negligible C_I in the triangular region bound by the red and white dashed lines. **c, d,** Same as **b** at 30 K and 50 K, respectively. Thermally assisted exciton injection is observed.

Extended Data Figure 8 | Circuit diagram. a, Circuit diagram for the penetration capacitance measurement. The red dashed line encloses the sample area. The reference (V_{ref} and C_{ref}) is used to cancel the parasitic background capacitance. The HEMT is biased at voltage V_H. **b,** Equivalent circuit model of C_P in **a**. Here $C_g \approx 2C_{gg}$ is the sample-to-gate geometrical capacitance, which is about twice the gate-to-gate geometrical capacitance C_{gg}.

Extended Data Figure 9 | Equivalent device circuit model for electrostatics simulation. $C_{Q,M}$ and $C_{Q,W}$ are the quantum capacitances of the $MoSe_2$ and WSe_2 monolayers, respectively. Details see Methods.

Extended Data Figure 10 | Exciton entropy analysis. a, Equation of state (chemical potential μ_X versus density n_X) for excitons at varying temperatures T. The data is

obtained by integrating the measured interlayer capacitance with respect to exciton density. **b,** Exciton chemical potential of **a**, replotted as a function of temperature at varying exciton densities. **c,** Entropy change per exciton, $\left(\frac{\partial S}{\partial n_X}\right)_T$, as a function of exciton density at varying temperatures (S denoting the 2D exciton entropy density). The data is obtained from **b** by applying the Maxwell's relation, $\left(\frac{\partial \mu_X}{\partial T}\right)_{n_X} = -\left(\frac{\partial S}{\partial n_X}\right)_T$. As density increases, $\left(\frac{\partial S}{\partial n_X}\right)_T$ drops rapidly, followed by a slow decrease. The crossover between the two regimes is correlated with the location of the compressibility peak in Fig. 4b of the main text. It corresponds to a crossover from a non-degenerate to a degenerate exciton fluid. In the latter, the density fluctuations are suppressed and the entropy change per exciton is substantially reduced. No entropic signature of the 2D superfluid transition is observed. A broad entropy peak is observed near the Mott density, reflecting the presence of a low-temperature Mott critical point. Only a high-temperature crossover is accessed here.

Figure 1

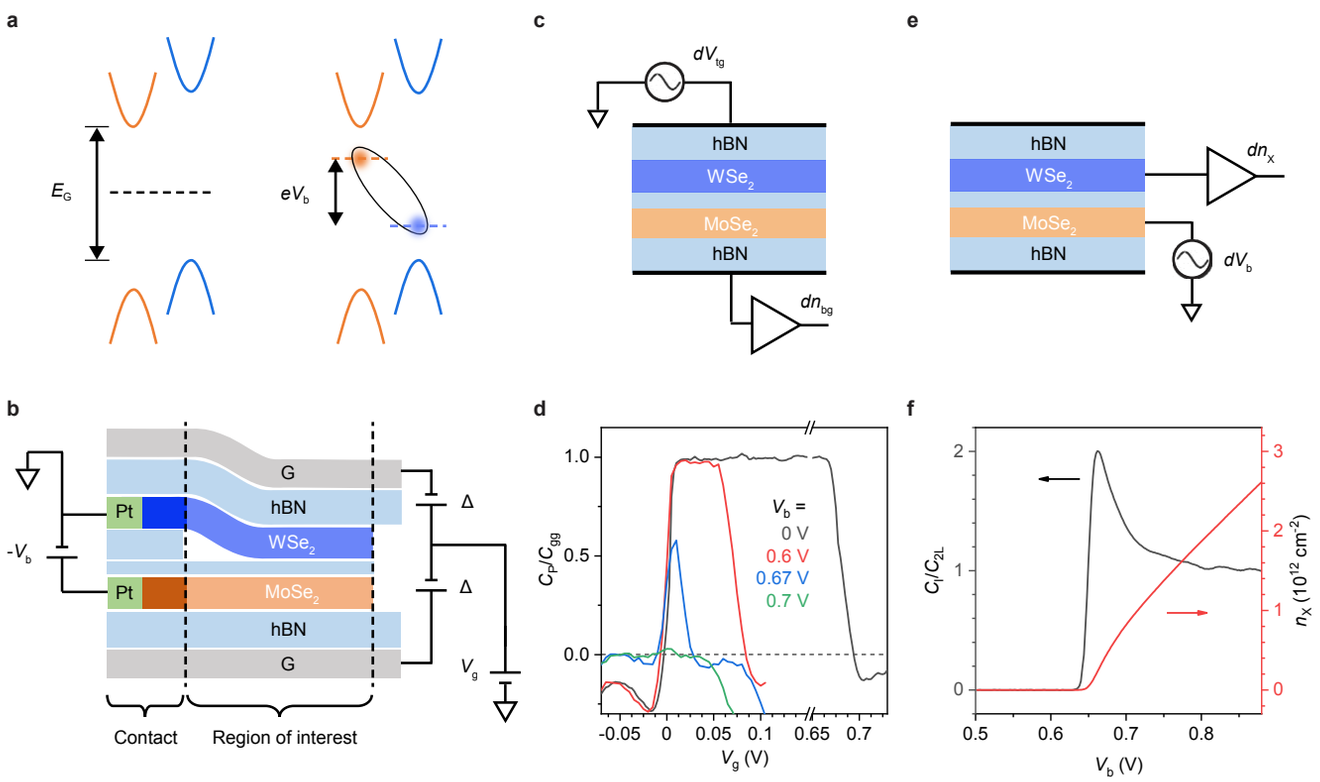
a
E_G
eV_b
c
dV_{tg}
hBN
WSe_2
$MoSe_2$
hBN
dn_{bg}
e
hBN
WSe_2
$MoSe_2$
hBN
dn_X
dV_b
b
G
hBN
WSe_2
Pt
Pt
$MoSe_2$
hBN
G
$-V_b$
Δ
Δ
V_g
Contact
Region of interest
d
C_P/C_{gg}
1.0
0.5
0.0
V_b =
0 V
0.6 V
0.67 V
0.7 V
-0.05
0
0.05
0.1
0.65
0.7
V_g (V)
f
C_I/C_{2L}
2
1
0
n_X (10^{12} cm^{-2})
3
2
1
0
0.5
0.6
0.7
0.8
V_b (V)

Figure 2

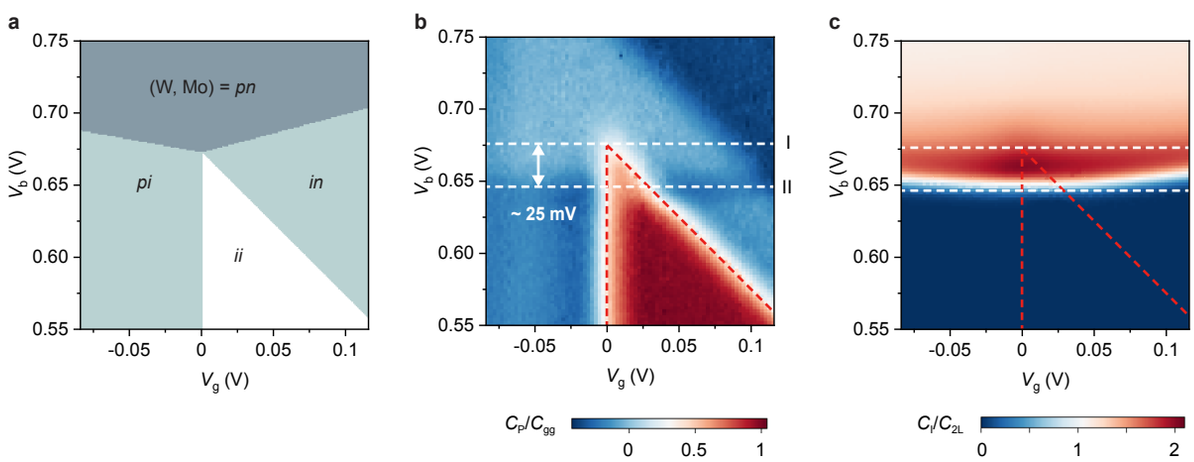
a
(W, Mo) = pn
pi
in
ii
0.75
0.70
0.65
0.60
0.55
V_b (V)
-0.05
0
0.05
0.1
V_g (V)
b
~ 25 mV
I
II
C_P/C_{gg}
0
0.5
1
c
C_I/C_{2L}
0
1
2

Figure 3

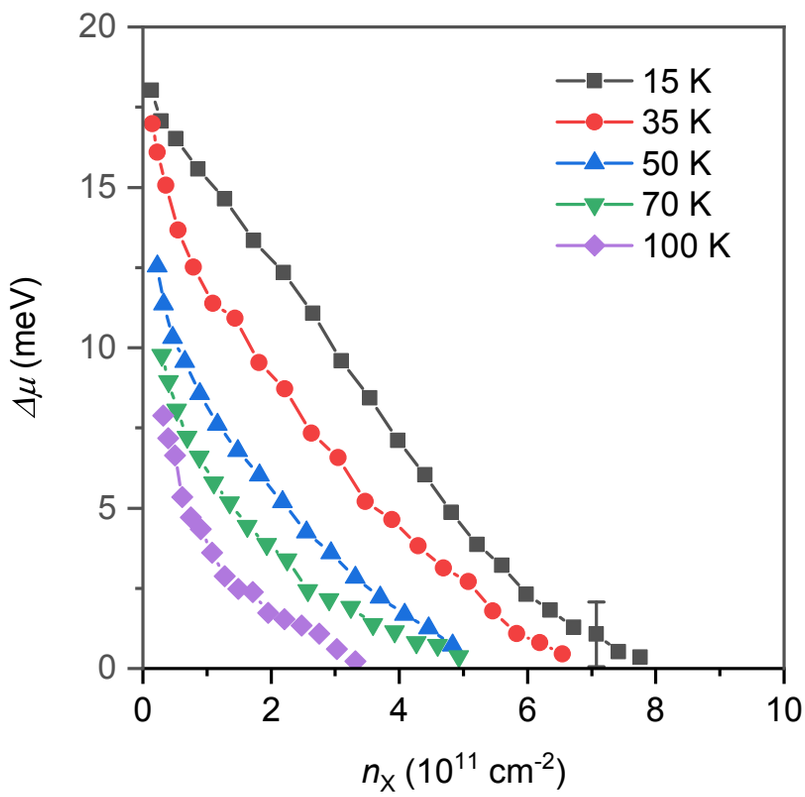

Figure 4

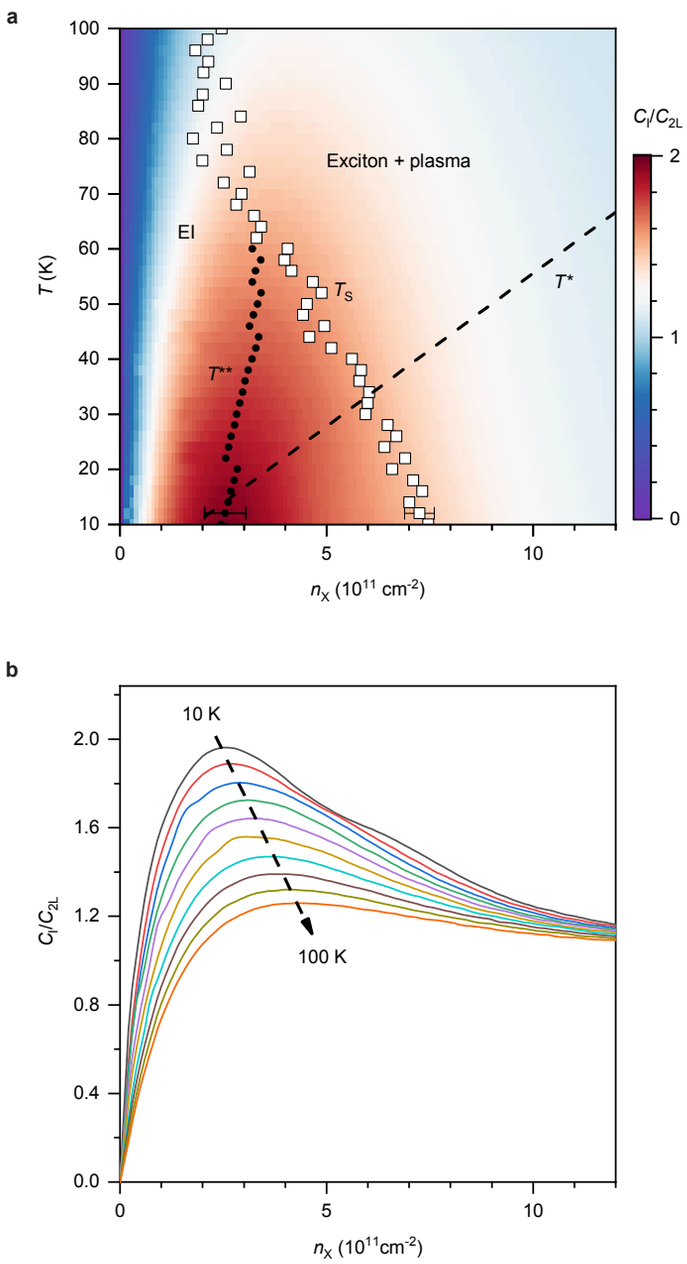
a
100
90
80
70
60
50
40
30
20
10
T (K)
0
5
10
n_X (10^11 cm^-2)
Exciton + plasma
EI
T_S
T*
T**
C_l/C_2L
2
1
0
b
2.0
1.6
1.2
0.8
0.4
0.0
C_l/C_2L
10 K
100 K
0
5
10
n_X (10^11cm^-2)

Ext Data Fig. 1

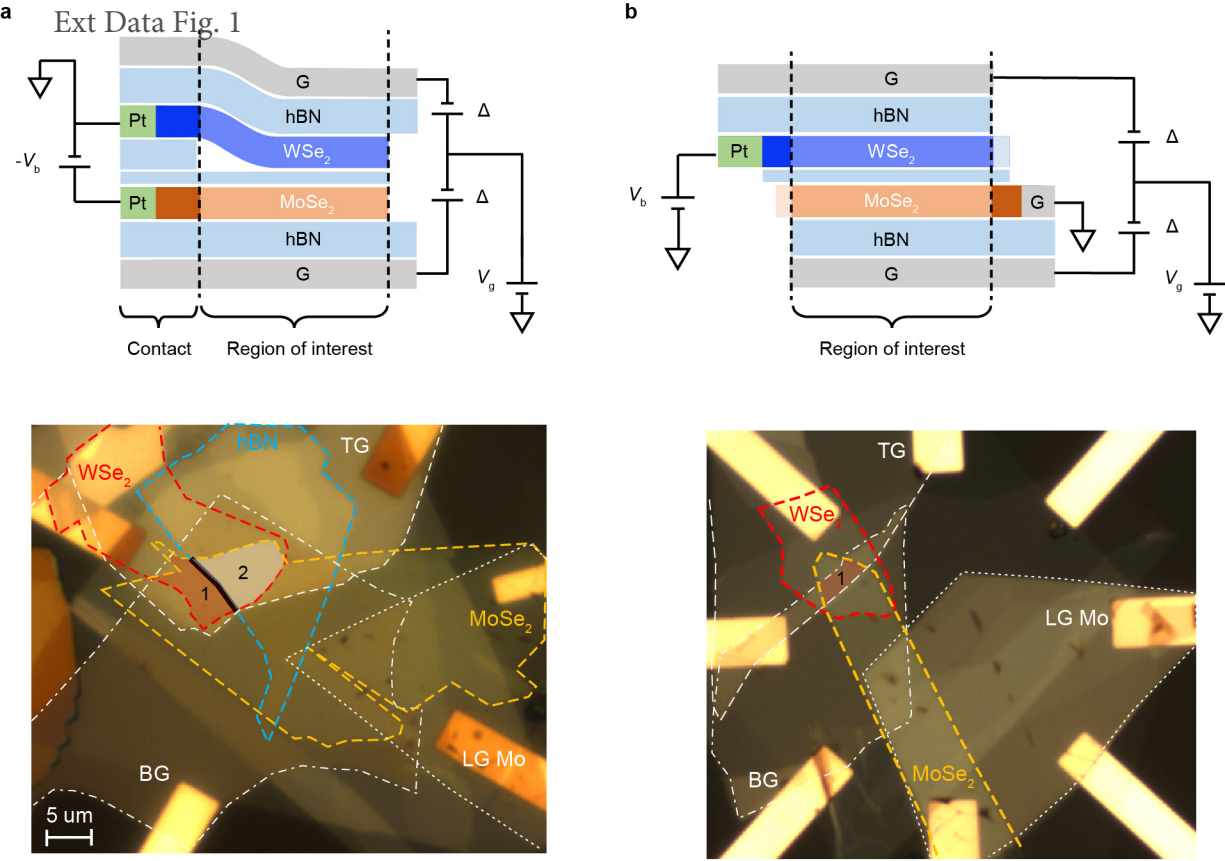

a Ext. Data Fig. 2

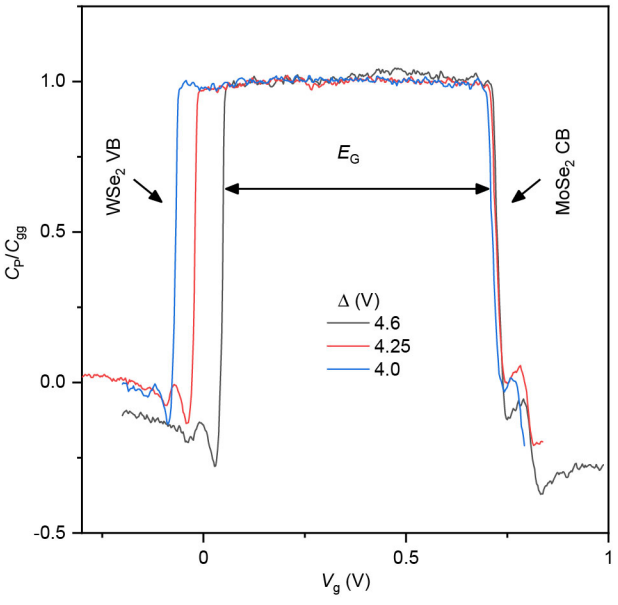

b

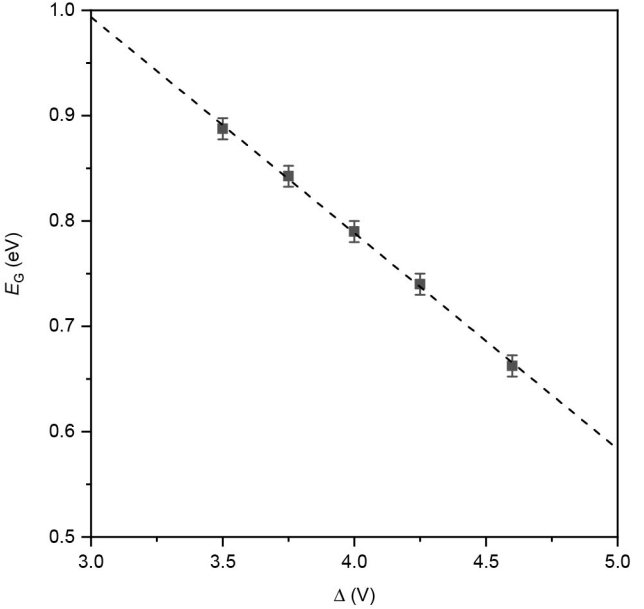

Ext. Data Fig. 3

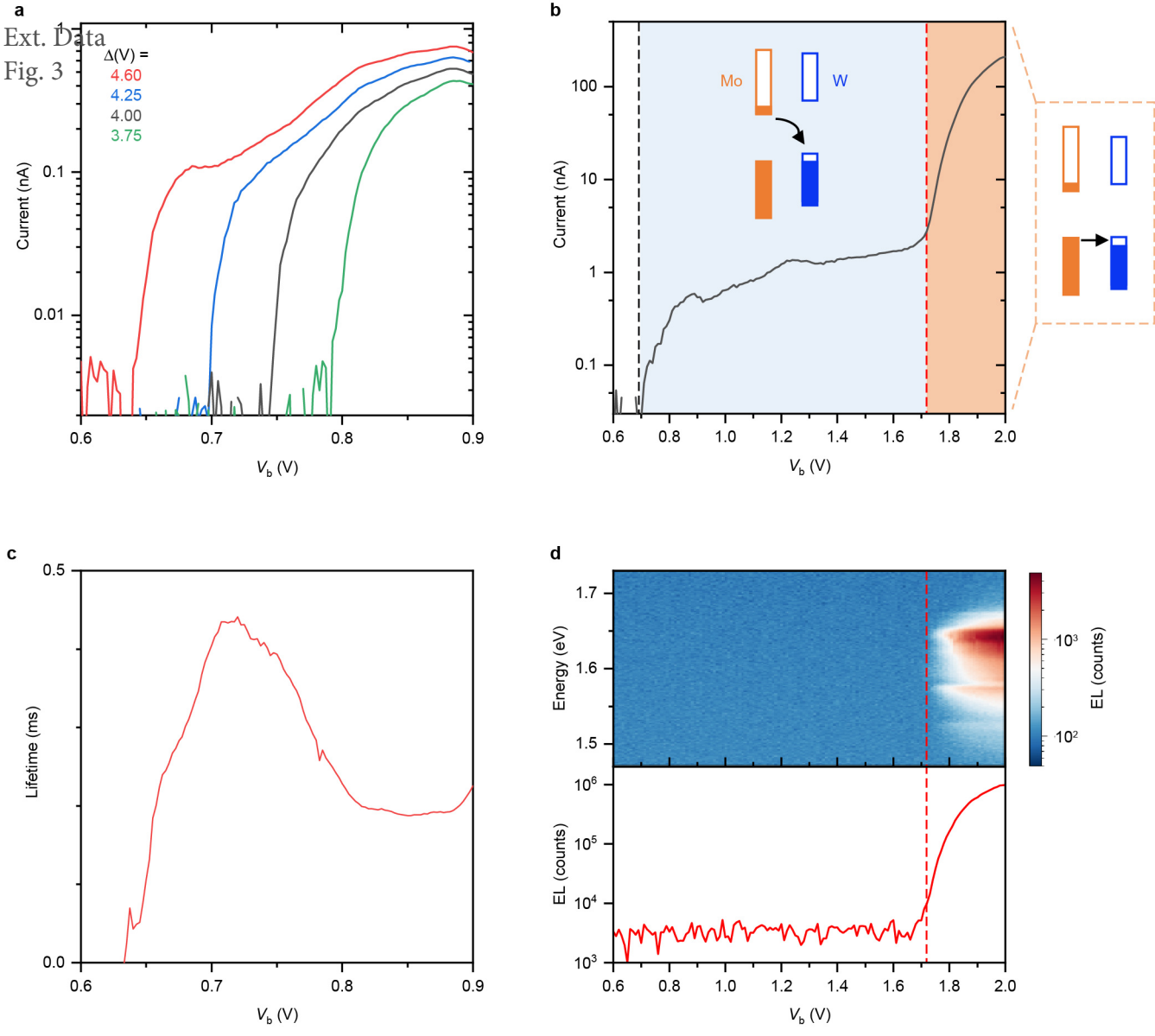

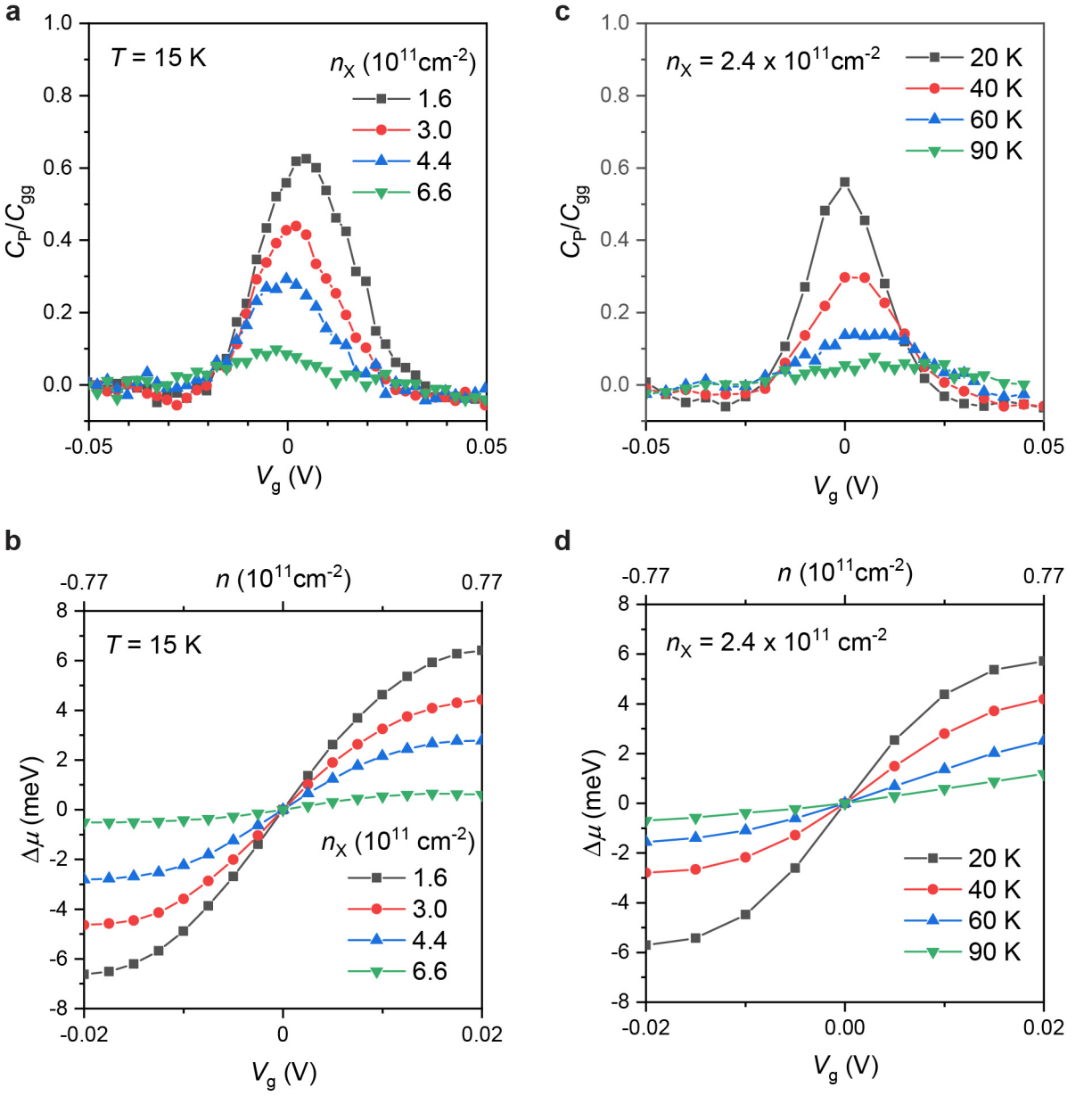
a
T = 15 K
n_X (10^11 cm^-2)
1.6
3.0
4.4
6.6
C_P/C_gg
V_g (V)
c
n_X = 2.4 x 10^11 cm^-2
20 K
40 K
60 K
90 K
C_P/C_gg
V_g (V)
b
T = 15 K
n (10^11 cm^-2)
n_X (10^11 cm^-2)
1.6
3.0
4.4
6.6
Δμ (meV)
V_g (V)
d
n_X = 2.4 x 10^11 cm^-2
n (10^11 cm^-2)
20 K
40 K
60 K
90 K
Δμ (meV)
V_g (V)

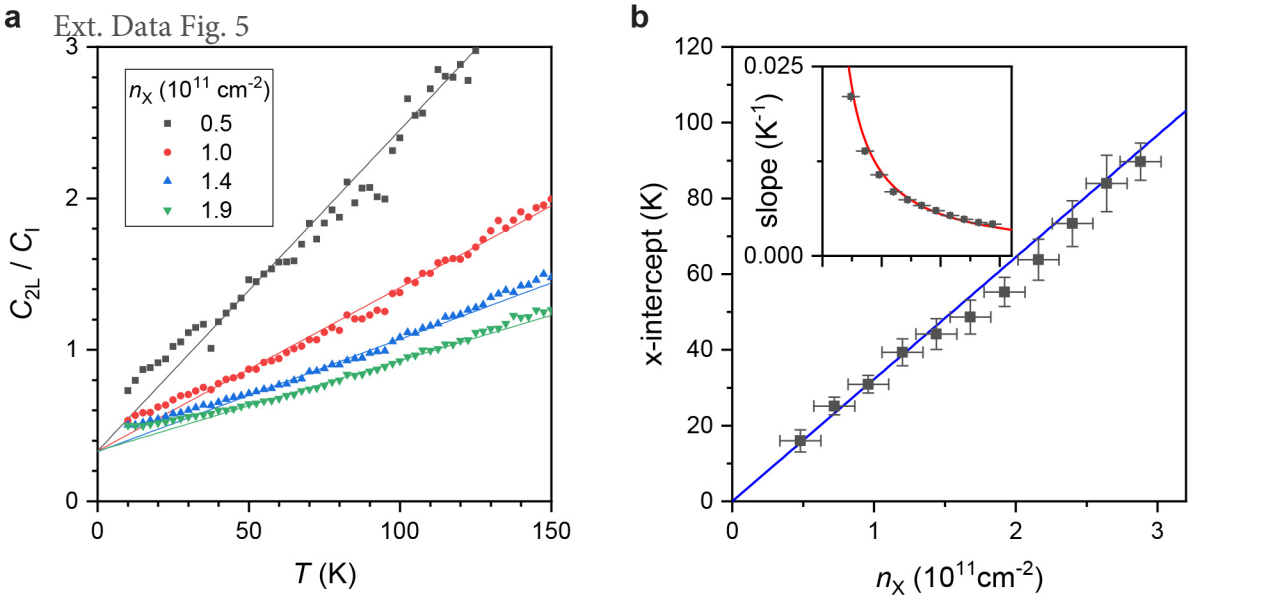
a
n_X (10^{11} cm^{-2})
0.5
1.0
1.4
1.9
C_{2L} / C_1
T (K)
0
50
100
150
1
2
3
b
x-intercept (K)
slope (K^{-1})
0.025
0.000
n_X (10^{11}cm^{-2})
0
20
40
60
80
100
120

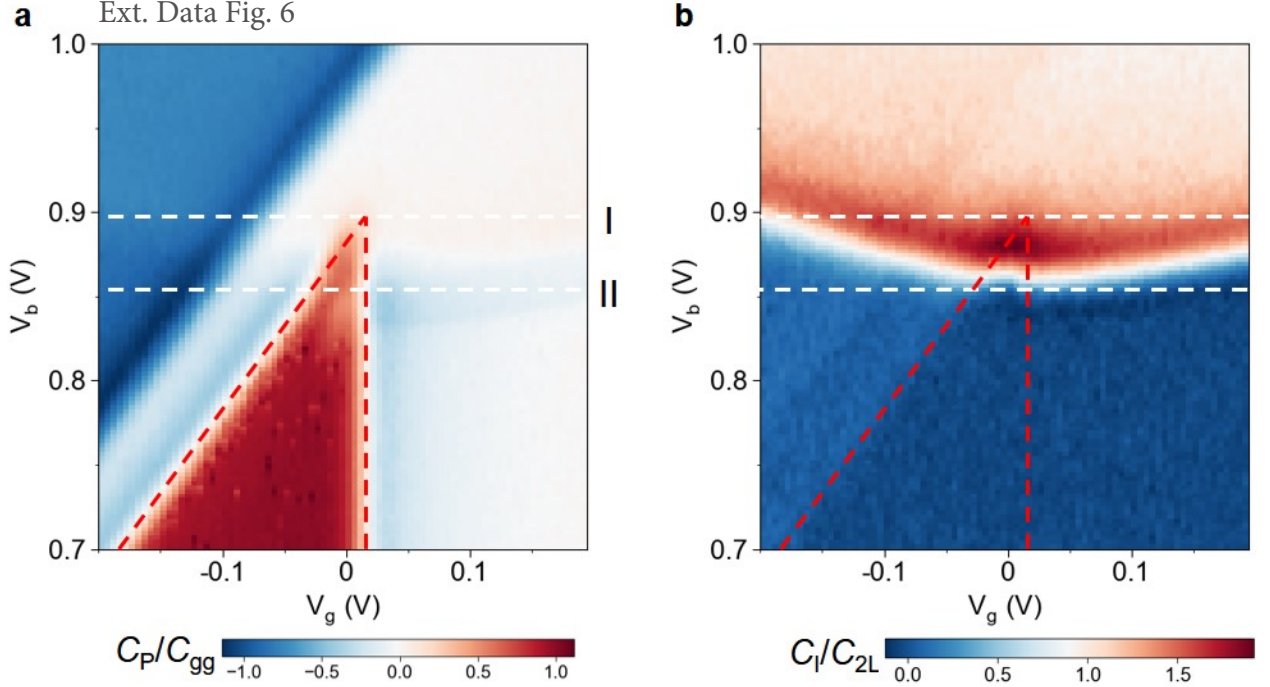
a
b
1.0
0.9
0.8
0.7
V_b (V)
I
II
-0.1
0
0.1
V_g (V)
C_P/C_{gg}
−1.0
−0.5
0.0
0.5
1.0
C_I/C_{2L}
0.0
0.5
1.0
1.5

Ext. Data Fig. 7

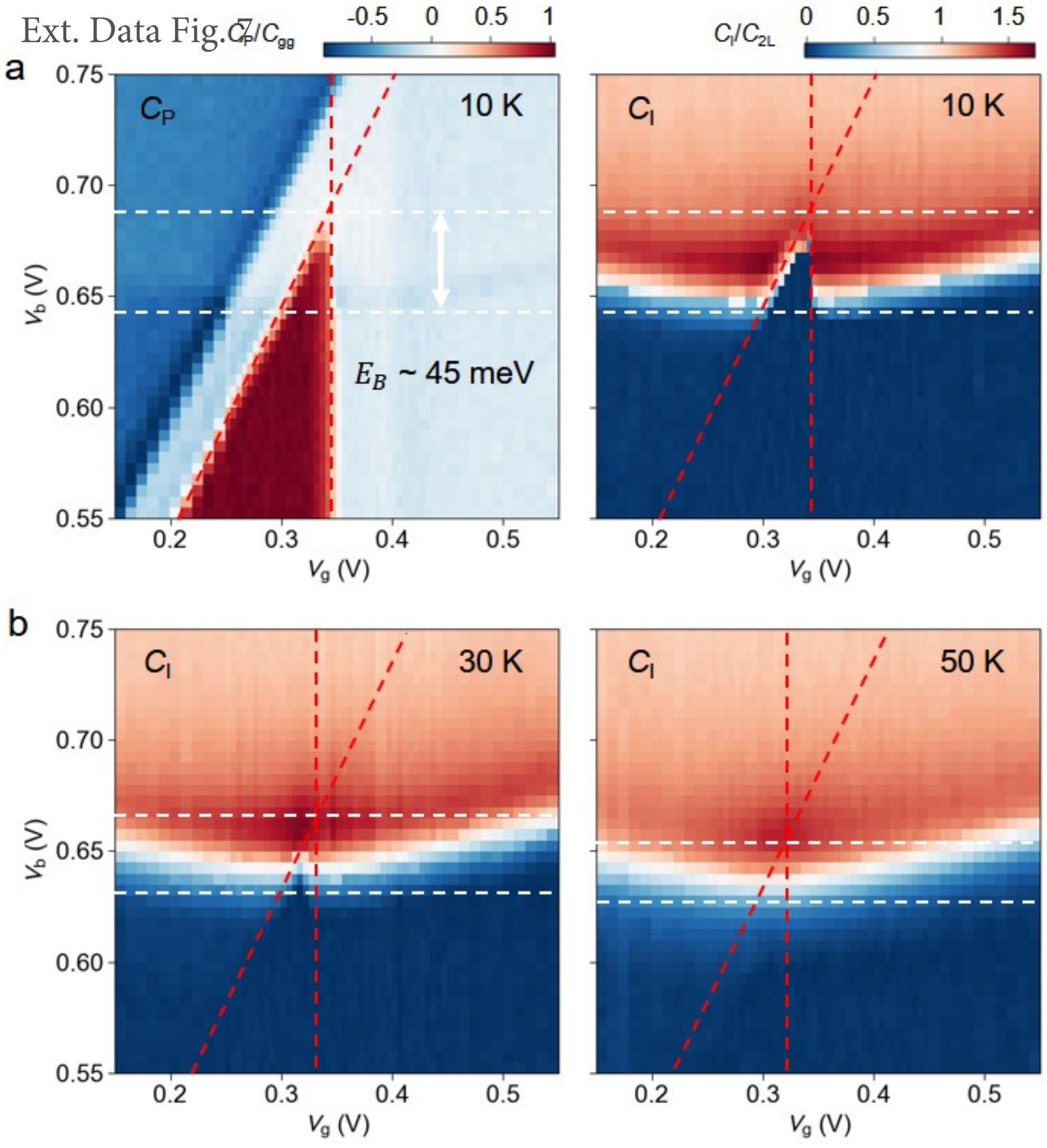

a Ext. Data Fig. 8

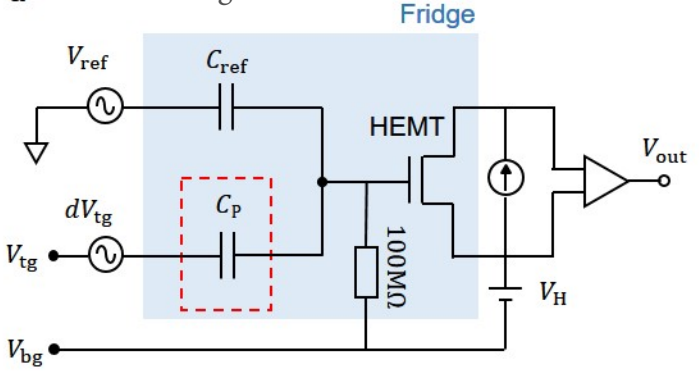

b

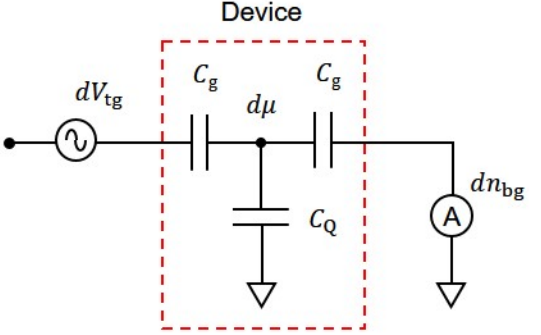

Ext. Data Fig. 9

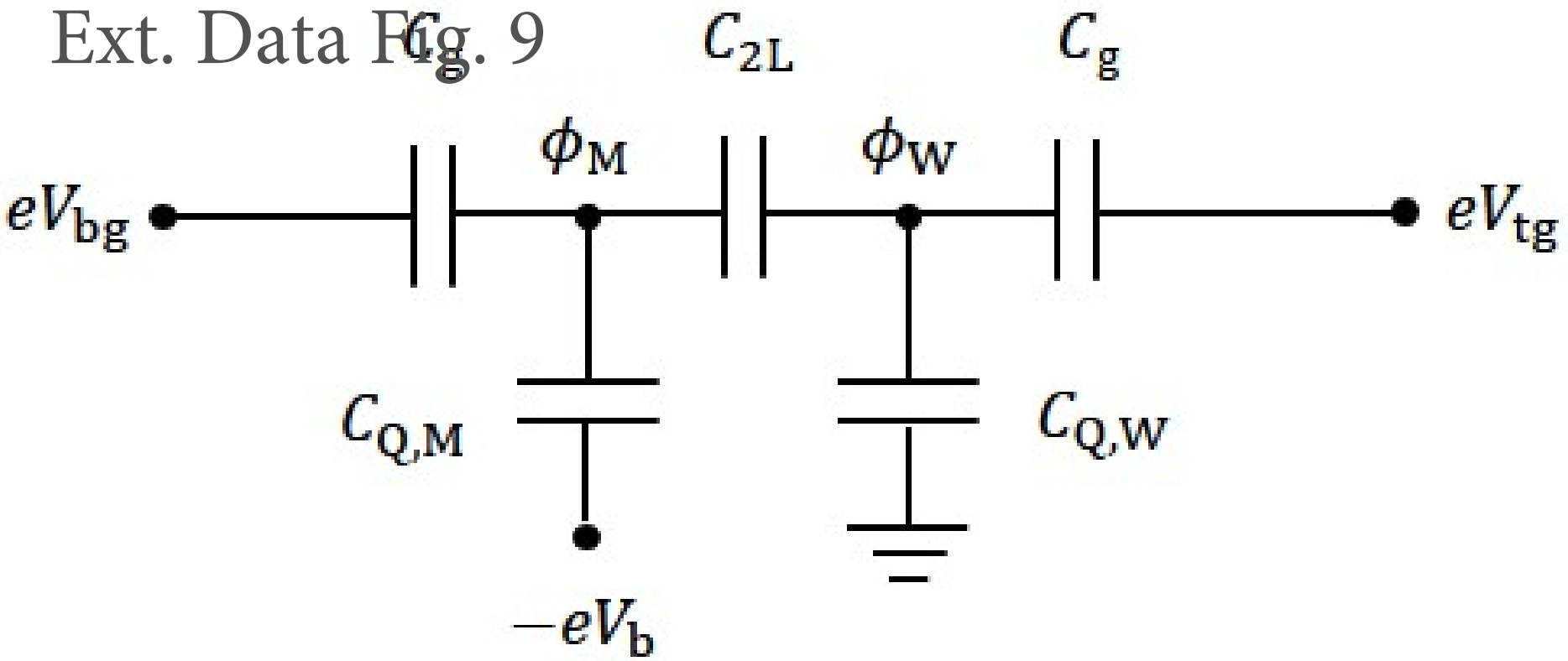

Ext. Data Fig. 10